



This open access document is published as a preprint in the Beilstein Archives with doi: 10.3762/bxiv.2020.19.v1 and is considered to be an early communication for feedback before peer review. Before citing this document, please check if a final, peer-reviewed version has been published in the Beilstein Journal of Nanotechnology.

This document is not formatted, has not undergone copyediting or typesetting, and may contain errors, unsubstantiated scientific claims or preliminary data.

Preprint Title 2D/2D Pomelo Peel Graphene/g-C₃N₄/Cu in situ for Enhancing Photocatalytic H₂ Production under Visible Light Irradiation

Authors Bingbiao Li, Zhixiong Xu and Heping Zeng

Publication Date 13 Feb 2020

Article Type Full Research Paper

ORCID® iDs Bingbiao Li - <https://orcid.org/0000-0002-4656-8721>

License and Terms: This document is copyright 2020 the Author(s); licensee Beilstein-Institut.

This is an open access publication under the terms of the Creative Commons Attribution License (<https://creativecommons.org/licenses/by/4.0>). Please note that the reuse, redistribution and reproduction in particular requires that the author(s) and source are credited.

The license is subject to the Beilstein Archives terms and conditions: <https://www.beilstein-archives.org/xiv/terms>.

The definitive version of this work can be found at: doi: <https://doi.org/10.3762/bxiv.2020.19.v1>

2D/2D *Pomelo Peel* Graphene/g-C₃N₄/Cu in situ for Enhancing Photocatalytic H₂ Production under Visible Light Irradiation

Bingbiao Li, Zhixiong Xu, Heping Zeng^{a,b*}

^a Key Laboratory of Functional Molecular Engineering of Guangdong Province, South China University of Technology, Guangzhou 510641, People's Republic of China.

^b Guangzhou Key Laboratory of Materials for Energy Conversion and Storage, School of Chemistry and Environment, South China Normal University, Guangzhou, 510006, P. R. China.

*Corresponding author. Tel.: +86-20-87112631; Fax: +86-20-87112631; E-mail:

hpzeng@scut.edu.cn

ABSTRACT

Pomelo peel was firstly used as the precursor with activating agent KHCO₃ to prepare few layered graphene nanosheets (GS) through gas stripping method. The precursor graphitized and transformed to few layered graphene nanosheets gradually because of the preset temperature program and KHCO₃. GS-4-1100, possessed the highest graphitization ($I_D/I_G = 0.14$, $I_{2D}/I_G = 0.923$) in 2~3 layers, at the edges. Taking advantages of the excellent electronic transmission performance and unique two-dimensional structure of both graphene and porous graphitic carbon nitride (g-C₃N₄), 2D/2D graphene/g-C₃N₄ nanosheet composite was fabricated for photocatalytic hydrogen evolution. The results showed that nano-copper (Cu NPs) performed the hydrogen evolution rate of 1.09 mmol g⁻¹ h⁻¹, while that of GS/CN-2 reached 2.91 mmol g⁻¹ h⁻¹ with *in situ* 5.49wt% Cu NPs. GS/CN-2/Cu turned out to be a stable and clean photocatalyst for hydrogen production.

KEYWORDS: g-C₃N₄, photocatalyst H₂ production, *pomelo peel* graphene nanosheets

INTRODUCTION

The development of clean renewable energy has attracted considerable concern because of the worsening environmental pollution and the shortage of energy. Hydrogen energy has the advantages of renewable and zero carbon emission with high energy conversion efficiency as one of the ideal energy sources.¹⁻⁶ As is well-known that photocatalytic hydrogen evolution is an effective way to deal with energy crisis and different kinds of environmental problems in the future. Graphene as a two-dimensional structure of carbon atoms in crystal has a very high specific surface area (2600 m² g⁻¹), excellent electrical conductivity and electron mobility (200000 s⁻¹ cm² V⁻¹), can effectively transfer light electrons or holes, reduce the composite of carrier. So, with the help of graphene's unique electronic transmission characteristics, photocatalytic materials prepared with semiconductor and graphene composite can significantly improve the efficiency of photocatalysis and is expected to play a role in energy and environmental protection.⁷⁻¹¹ It has been reported that graphene combined with g-C₃N₄ can enhance the photoconversion efficiency of the material and therefore promote the performance photocatalytic hydrogen production.¹²⁻²¹ In these composite catalytic systems, graphene reduces recombination rate of the electron-hole pair and also prevents semiconductor aggregation to some degree as an electron transfer substrate, which greatly improves the photocatalytic performance of the system.²²⁻²⁴

Furthermore, graphitized carbonitride (g-C₃N₄) is a kind of carbon-based materials, which has been proved to be efficient and versatile supporting materials in recent years. Nitrite is one of the most promising surface modification materials with good chemical stability, thermal stability, low

density, super hardness, water resistance and biocompatibility.^{6, 19, 21, 25-28} In addition, because these materials are easy to prepare, they are of reference value compared with other contemporary scaffolds. Normally during the synthesis of g-C₃N₄, the precursors are thermochemically decomposed into porous materials with high surface areas. It is worth noting that g-C₃N₄ is an inherently photoactive material with a suitable band gap of 2.73 eV,²⁹⁻³⁰ so it is expected to be widely used in a wide range of applications, including visco-mediated conversion.

In recent years, graphite oxide reduction,³¹⁻³³ chemical vapor deposition (CVD),³⁴⁻³⁷ epitaxial growth^{3, 38-39} and other methods⁴⁰⁻⁴² have been reported for graphene synthesis. However, these methods are too time-consuming and not environmental to produce high-quality graphene on a large scale. Biomass waste is cheap, non-toxic and abundant to prepare graphene, which meets the need of successfully synthesize graphene in a simple and environment friendly way and has attracted increasing attention. Therefore, reliable biomass precursors are the key to explore simple and reliable methods for graphene nanosheet synthesis. Up to now, some kinds of regenerate biomass have been utilized as precursors to synthesize graphene nanosheets, biomass tar⁴³, agricultural and forestry residues⁴⁴, spruce bark⁴⁵ and kelp⁴⁶ included. Moreover, KOH has been utilizing widespread as activating agent for developing graphene^{45, 47-49}, generating the porous structure with different carbon precursor with complicated reaction process. However, it's likely to mix the carbon material in KOH solution to ensure mixing well due to the deliquescence of KOH. Thus, oxygen content in the product reaches higher level after complicated reaction process. Instead, using activating agent KHCO₃ can improve carbon content of graphene and simplify the reaction process and may result in more environmental and efficient synthesis of biomass-derived few layered graphene in large scale.

In this work, *pomelo peel* was firstly chosen as the raw material to synthesis few layered graphene nanosheets (GS) by gas stripping method with KHCO₃ as activating agent. The mixture constantly exfoliated into released gas(CO、H₂O and CO₂) and collapsed, contributing to the preset temperature control program and activating agent KHCO₃. Based on our previous work⁵⁰⁻⁵⁵, 2D/2D graphene/g-C₃N₄ (GS/CN) nanosheet was developed with the prepared few layered graphene nanosheets by above process and melamine in popular ways to further improve their performance of hydrogen evolution. Moreover, the influence of the graphitization temperature and the ratio between the *pomelo peel* and activating agent KHCO₃) on the graphitization were conducted systematic research. To measure the photocatalytic efficiency of GS/CN, an efficient and convenient in situ method was performed to generate the copper nanoparticles (Cu NPs) with lactic acid as sacrificial electron donor under visible light in vacuum environment. GS/CN-2/Cu performed highest hydrogen evolution rate and steady activity in photocatalytic H₂ evolution circulation.

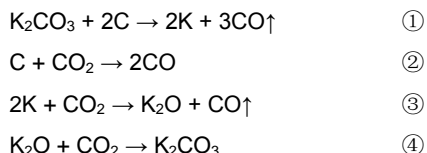
Results and discussion

Preparation process and characterization of GS

In the whole synthetic process, *pomelo peel* was the carbon precursor while KHCO₃ was the activating agent caused the graphitization and carbonization of the samples. KHCO₃ began to decompose to K₂CO₃, H₂O and CO₂ rapidly till 262.4 °C.⁵⁶ Afterwards, K₂CO₃ was decomposed to K₂O and CO₂ when the temperature is above 700 °C. The intermediate product CO₂ would be reduced by C to release CO while K₂CO₃ reacted with C and produced K and CO. According to Eq. ①③④, the rich K solid in the samples could take part in the reduction–oxidation cycles, during which carbon materials were etched constantly.⁵⁷ There was a lot of gas released out, causing homogeneous and continuous corrosion and leading to rich micro/mesoporous and layered

amorphous structure at the same time. The gas further intercalated into the carbon lattice by overcoming the van der Waals attraction, resulting in an in-situ synergic exfoliation in the time of graphitization. Additionally, the K generated in the REDOX reaction is effectively embedded in the carbon lattice, resulting in the carbon lattice expansion during the activation process.⁵⁸ The samples irreversibly collapsed and shrank due to the high temperature and the heavy consumption of raw materials, having great impact on the microscopic morphology and increasing the graphitization degree and specific surface furtherly.

As shown in **Fig 1 (a)**, Raman spectroscopy was carried out to characterize the graphitization and crystallinity degree of the samples. Three characteristic peaks of graphene showed in the



Raman spectra were summarized, including D band, G band and 2D band, respectively.³⁷ The peak D at about 1330 cm^{-1} , originated from the breathing pattern of outerplanar vibration of disordered sp^3 -bonded carbon atoms, was used to characterize structural defects at the edge of or in graphene samples. The peak G at approximately 1590 cm^{-1} ascribed to the in-plane vibration of sp^2 -hybridized carbon atoms in a two-dimensional hexagonal lattice. The G band can effectively reflect the number of graphene layers and be highly susceptible to stress. The peak 2D at near 2690 cm^{-1} caused by the second order of zone-boundary phonons and was sensitive to stacking of graphene nanosheets.³⁷ Generally, the intensity ratio of D band to G band (I_D/I_G) was applied to characterize the defect density or degree of ordering of graphene.³²

With higher mixing ratio of activating agent, the I_D/I_G values became no more than 0.20 because graphene would be corroded and collapse from large scale to pieces with plenty of activating agent, leading to structural collapse and a mass of defect irreversibly. The I_D/I_G values of GS-2-1100, GS-3-1100, GS-4-1100, GS-5-1100 and GS-6-1100 were 1.07, 0.61, 0.14, 0.17 and 0.20, respectively, indicating that full dose of activating agent corroded graphene into fragments and results in large area defects and irreversible structural collapse of graphene ensured good crystallinity and ordering micro-structure of the graphene nanosheets.³² The intensity ratio of G to 2D band (I_G/I_{2D}) of GS-6-1100 was 1.006, indicating highest graphitization degree and least layers (≤ 3 layers) feature among GS-X-1100 while that of GS-4-1100, GS-5-1100 were 1.015 and 1.128 respectively.⁵⁹ However, the yield of GS-4-1100 was 21.5% while GS-6-1100 with 5.06% in yield only. For environmental consideration, GS-4-1100 were chosen to further study the influence of calcination temperature on the structure of graphene, but not GS-6-1100 with a little higher I_G/I_{2D} values. Obviously, as shown in **Fig 1 (b)**, I_G/I_{2D} values increased whether the calcination temperature was higher or lower, indicating that 1100°C was the appropriate calcination temperature for KHCO_3 to activating the carbon precursor to be graphitized and from ordered structure.

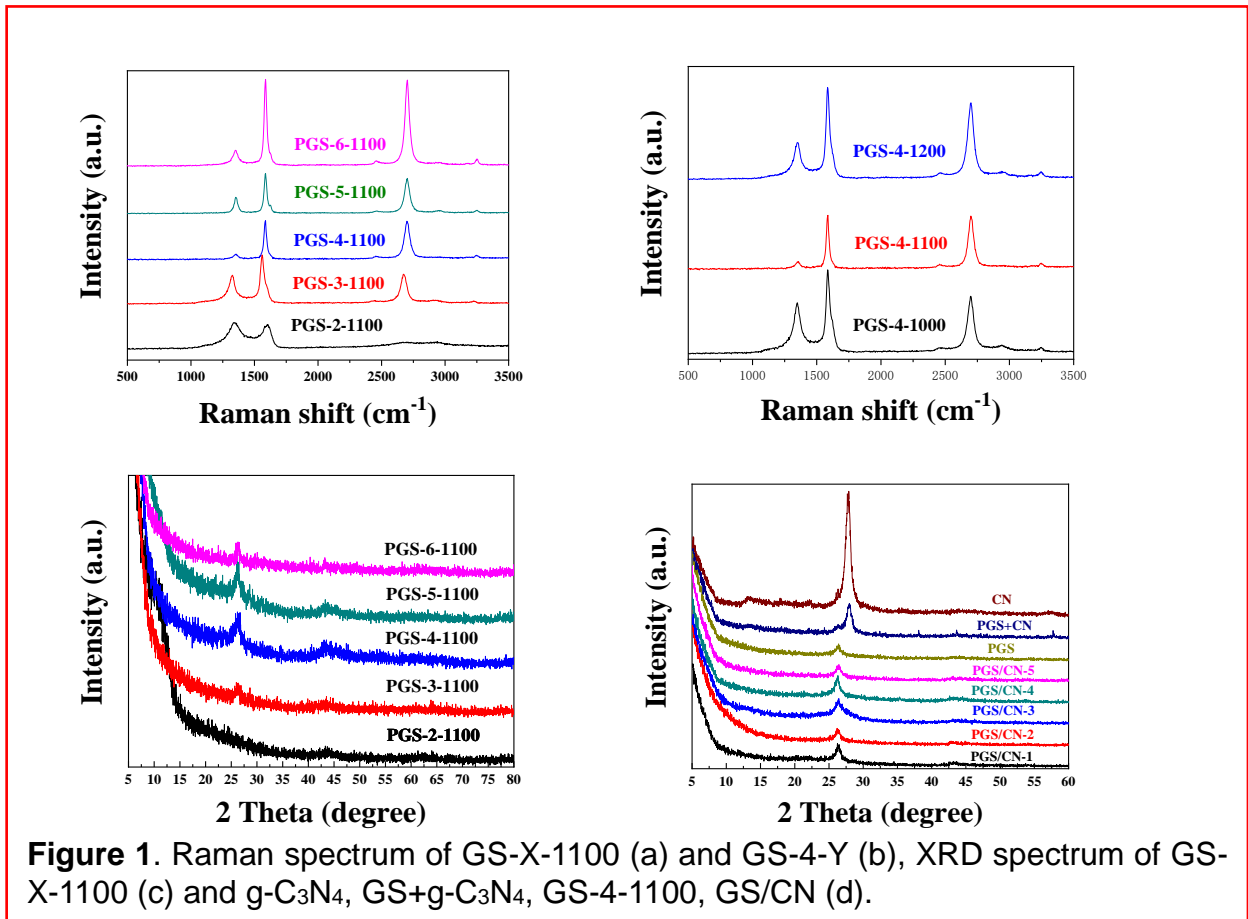


Figure 1. Raman spectrum of GS-X-1100 (a) and GS-4-Y (b), XRD spectrum of GS-X-1100 (c) and g-C₃N₄, GS+g-C₃N₄, GS-4-1100, GS/CN (d).

Fig. 1(c), showed the X-ray diffraction (XRD) patterns of GS-X-1100, among which GS-4-1100 and GS-5-1100 hold greater crystallinity degree, indicating that plenty of potassium hydroxide has distinct impact on the graphitization of GS. However, GS-6-1100 appeared to display weak and sharp peak locating 26°, indexed as the (002) plane of graphene, with high degree of graphitization and almost invisible peak at 43.1°, indexed as the (101) plane of graphene, possibly caused by the corrosion of excess activating agent.⁶⁰⁻⁶¹ The XRD results coincided with the Raman's patterns that adequate activating agent contribute to high graphitization. In **Fig 1(d)**, the characteristic peak of g-C₃N₄ at 27.8°, corresponding to the superimposed reflection (002) plane between the layers of C₃N₄ conjugated aromatic system, could not be observed in the XRD patterns of GS/CN compared to sample g-C₃N₄ and GS+g-C₃N₄. GS may possess far better crystal form than g-C₃N₄ or the characteristic peak of g-C₃N₄ drifted into the peak at 26° in GS/CN due to the influence of GS-4-1100.

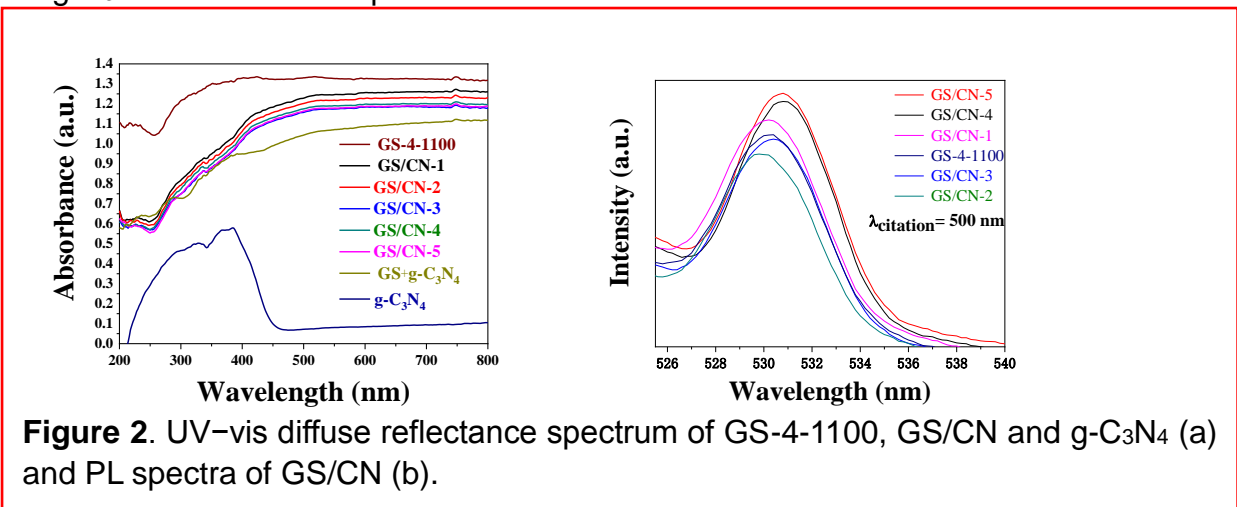
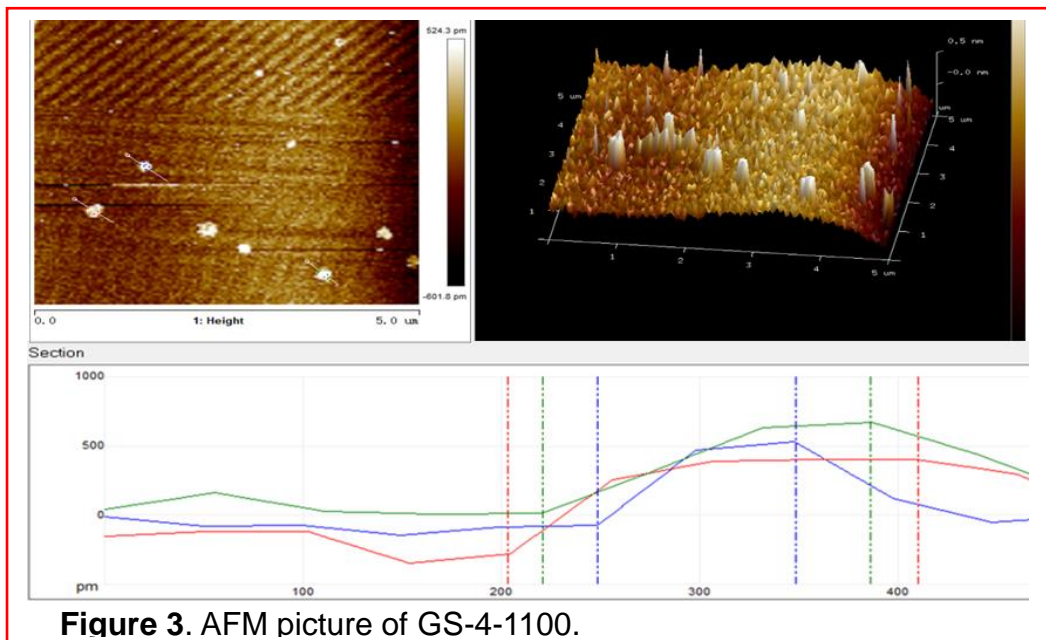


Figure 2. UV-vis diffuse reflectance spectrum of GS-4-1100, GS/CN and g-C₃N₄ (a) and PL spectra of GS/CN (b).

To evaluate the light-absorbing capacity properties and verify the photocatalytic activity of samples,

UV-vis absorption spectra were measured (**Fig 2 (a)**). The UV-vis patterns of GS-4-1100 and GS/CN obviously had higher absorption intensity than that of g-C₃N₄. The absorption intensity of the physical mixture GS+g-C₃N₄, consisted of GS-4-1100 and g-C₃N₄ in a ratio of 5:4 (mentioned above in section GS/CN nanosheets synthetic procedures), was only slightly less that of above two. The UV-vis absorption spectra showed that GS-4-1100 successfully improved the capacity of light absorption of g-C₃N₄ and GS/CN performed better, especially range ultraviolet to infrared region. The result was bound up with the high graphitization of GS-4-1100, as a photosensitizer, enlarging the absorption



range and improving the absorption capacity.⁶² However, the low absorption of g-C₃N₄, mixed in GS+g-C₃N₄, range ultraviolet to infrared region is not conducive to the separation of photogenerated electrons and holes, resulting in the low efficiency of GS+g-C₃N₄ in hydrogen evolution.

Photoluminescence (PL) spectra shown in **Fig 2 (b)** was measured under 500 nm exciting light to explore the crucial factor affecting the hydrogen evolution rate, the separation efficiency of electron hole pair in nanocomposites. Generally, carrier recombination rate is positively correlated with PL emission intensity while the electron-hole pairs lifetime is opposite.⁶³ GS/CN showed a distinct fluorescent band around 531 nm and there was a small gap between each other in the spectrum. The GS/CN-2 showed lowest fluorescence intensity, suggesting that it could possess highest charge transfer rate and maximum electron-hole pairs life span and could perform best photocatalysis activity for hydrogen generation.

Atomic force microscopy (AFM) patterns showed in **Fig 3** revealed the cross-sectional thickness of GS-4-1100 in the randomly selected area with a vertical distance at approximately 0.7 nm. Since the reported height of mono layer graphene was ~0.34 nm, GS-4-1100 should be 2~3 layered graphene contained abundant 2 layers characteristic at the edges, which coincided perfectly with

the Raman results discussed above.⁵⁹

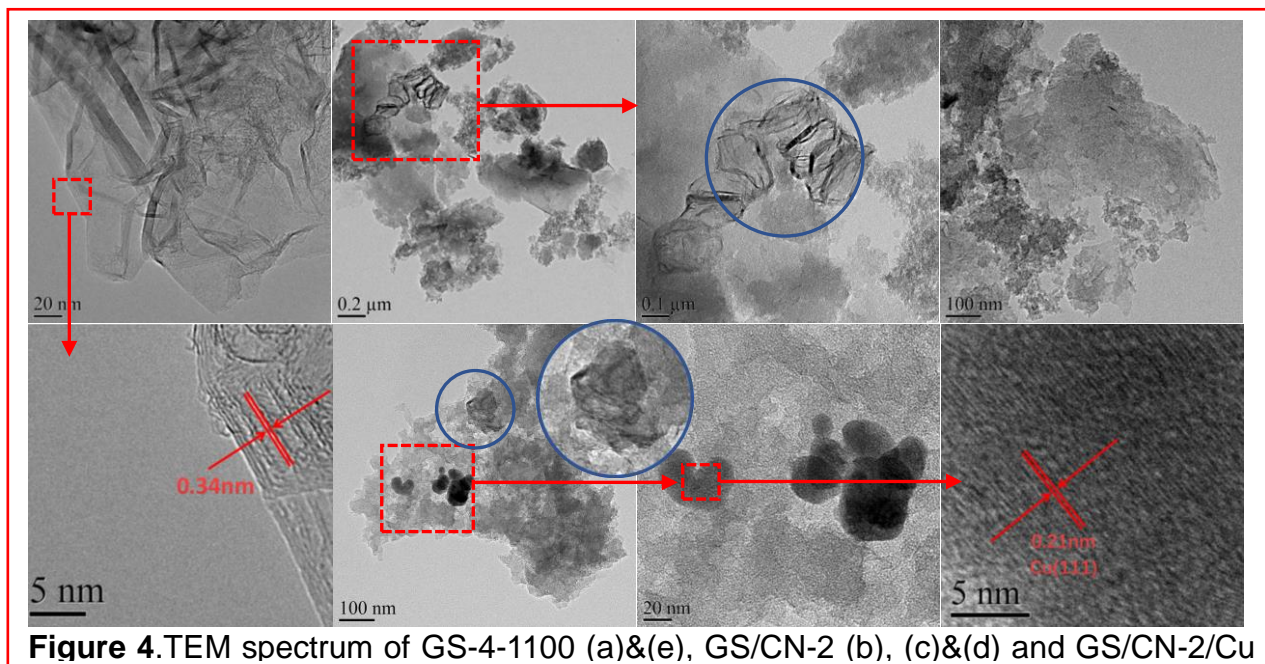


Figure 4. TEM spectrum of GS-4-1100 (a)&(e), GS/CN-2 (b), (c)&(d) and GS/CN-2/Cu

Fig 4(a)&(e) revealed the high-resolution TEM (HRTEM) patterns of GS-4-1100, clearly showing the characteristic of graphene in few layers (typically 2 or 3 layers at the edges), between which the interlayer distance was 0.348 nm. And the thickness of single layer graphene was well known as 0.34nm.⁶⁴ The result was coincided with the relative discussion in all experimental results above. As shown in **Fig 4(b)&(c)**, the irregular polygon shown in the TEM images of GS/CN-2 should be the original microstructure of *pomelo peel*, which was also discovered in the HRTEM patterns shown in **Fig 4(f)**. The overlapping 2D nanosheets of graphene and g-C₃N₄ layered upon layers, suggesting that graphene and g-C₃N₄ were synthesized into multi-layer stacks in 2D/2D structure.⁶⁵ Diaphanous layered structure emerged distinctly by introducing 2D g-C₃N₄ nanosheets, which was also observed in HRTEM patterns of GS/CN-2/Cu. The solid materials in the reactor were collected after photocatalytic hydrogen evolution continued for 3 h. The TEM images of the graphene nanosheets in different magnification with Cu nanoparticles adhered revealed that the lattice spacing was 0.21 nm, corresponding to the (111) plane of metallic Cu. In addition, some Cu nanoparticles became reunited in the right of **Fig 4(g)**, indicating that Cu NPs successfully formed in situ during the photocatalytic process.⁶⁶

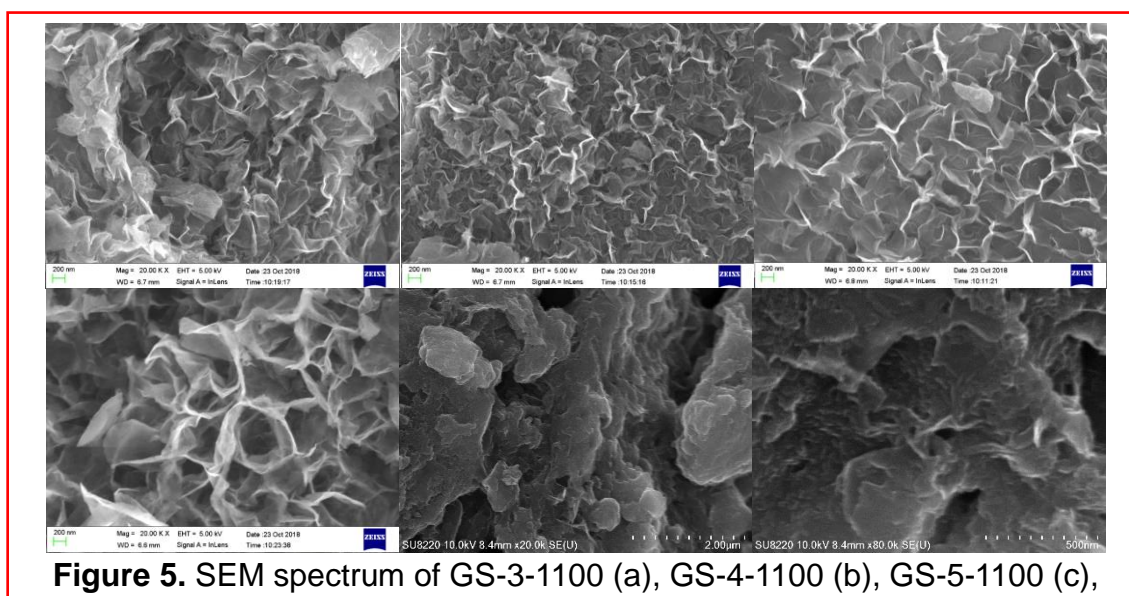


Figure 5. SEM spectrum of GS-3-1100 (a), GS-4-1100 (b), GS-5-1100 (c),

Scanning electron microscopy (SEM) was carried out to characterize the microstructures and morphology features of the samples. In **Fig 5** SEM patterns showed regular microstructures of GS-X-1100, demonstrating porous hexagonal ring honeycomb layered structure wrinkled in fold randomly and distinctly. And the influence of different addition of KHCO_3 on graphene nanosheets was also discovered. *Pomelo peel*, the original material corroded by KHCO_3 , could proceed carbonization and graphitization to form elementary porous structure and gradually enlarged to mesopores during the synthesis reaction. The SEM images revealed that the amount of pore reach the maximum as the mass ratios of activating agent KHCO_3 to carbonized materials was 4:1 at the same activating temperature, offering abundant active sites and minimizing the distance of ion diffusion.⁴² Less KHCO_3 added was inadequacy to graphitize the carbonized materials while excessive activating agent caused larger pores and less reactive site per unit area. As shown in **Fig 5(e)&(f)**, lamellar structure in GS/CN-2 taking shape as the wall of the holes was unfolding, widely covering the surface of graphene nanosheets. Such lamellar structure suggesting that graphene and g- C_3N_4 were synthesized into multi-layer stacks.

Photocatalytic Hydrogen Evolution.

The photocatalytic hydrogen evolution was performed in the lactic acid aqueous solution, irradiated by Xe lamp in visible light. GS-4-1100 mentioned above possessed the highest level of graphitization and Cu/GS-4-1100 performed well in the hydrogen evolution ($0.97 \text{ mmol g}^{-1} \text{ h}^{-1}$) in the standard case. The influence of the content of GS in GS/CN were performed with GS-4-1100 in the standard case. The result showed in **Fig 6(a)** revealed that the hydrogen evolution rate of GS/CN-2/Cu was the highest one ($2.05 \text{ mmol g}^{-1} \text{ h}^{-1}$) at 57.1% of the GS content in GS/CN. The outstanding GS/CN-2 sample with about half GS content performed best in the hydrogen evolution measurement, indicating that the equivalent raw material melamine may transform into sandwich-like structure in GS/CN. For reference, the relatively low performance of g- C_3N_4 and GS+g- C_3N_4 in the hydrogen evolution measurement **Fig 6(b)**, caused by low absorption of g- C_3N_4 range ultraviolet to infrared region, could be the evidence for the above argument. As shown in **Fig 6(c)**, with the rising volume of copper acetate, the hydrogen release rate of GS/CN-2/Cu reached the maximum ($2.91 \text{ mmol g}^{-1} \text{ h}^{-1}$) at 5.49wt% of the theoretical content of copper acetate. As the content of copper acetate increased, the excessive amount of copper NPs caused agglomeration and further increased the particle size of Cu NPs, going against the separation of the pore and electrons, resulting in a low rate of hydrogen evolution. GS/CN-2 had no photocatalytic activity, showing that GS/CN-2 did not produce photoelectrons. Besides, the hydrogen evolution rate of Cu NPs and GS-4-1100 was relatively low ($1.00 \text{ mmol g}^{-1} \text{ h}^{-1}$ and $0.97 \text{ mmol g}^{-1} \text{ h}^{-1}$ respectively) while that of other GS/CN samples were higher. Obviously, taking advantage of high graphitization, graphene acted as an electronic conductive channel in the composite catalyst, thus effectively facilitating the separation of photogenic carriers. These results contributed to the rapid transfer of photoelectrons from Cu NPs to the edge of GS/CN-2, inhibiting the recombination of photoelectron pairs. Meanwhile, Cu NPs spread over GS/CN-2 and thus avoided the agglomeration of Cu NPs.

The life of photocatalyst was one of its main characteristics. Under the standard conditions, the cyclic stability of GS/CN-2 was performed under visible light irradiation through 5 consecutive accumulations for 30 h in total. **Fig 6(d)**. Remarkably, due to the reduction of GS/CN-2, the reusing activity gradually increased, becoming a photocatalyst to promote water decomposition and improve electrical conductivity. The results showed that the GS/CN-2 performed remarkable photocatalysis stability.

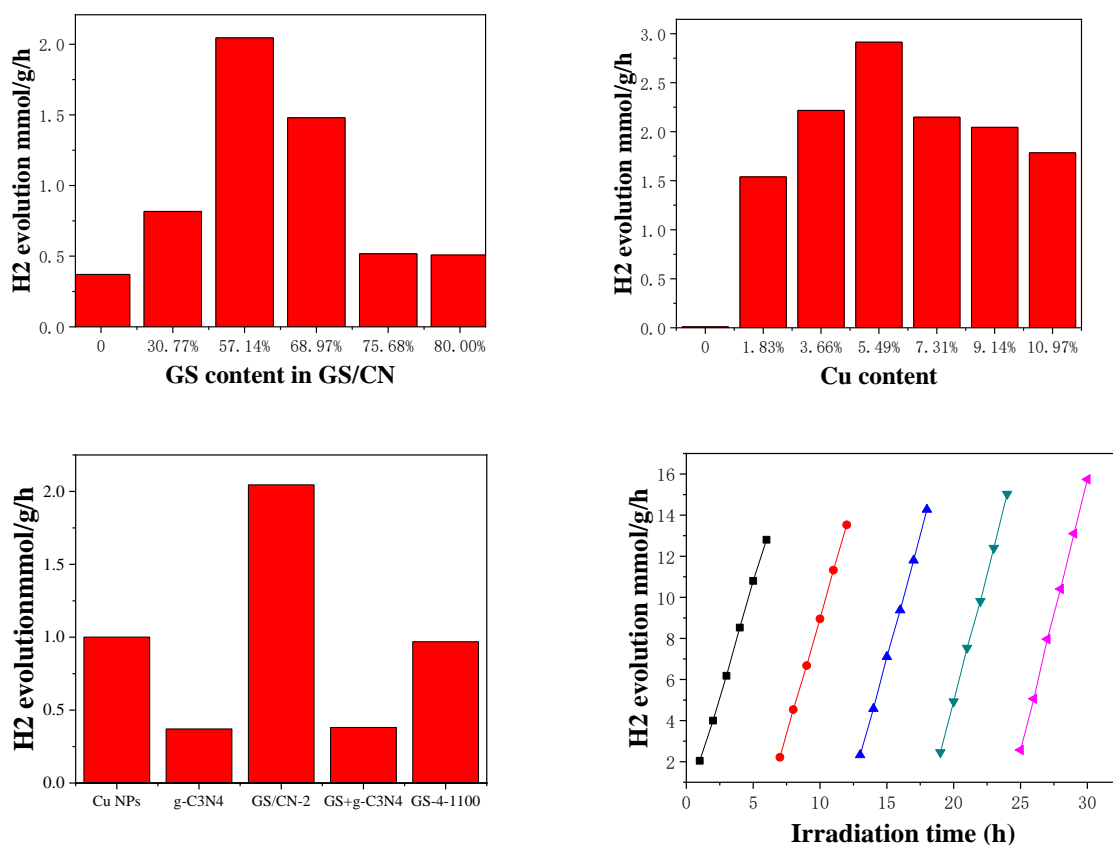


Figure 6. H₂ evolution rate of GS and GS/CN (a), GS/CN-2 with different Cu content (b), g-C₃N₄, GS-4-1100, GS/CN-2 and GS+g-C₃N₄ (c) and photocatalytic H₂ evolution circulation of GS/CN-2 in standard case for 30 h in total (d).

Conclusion

In general, few layered graphene nanosheets was explored with *pomelo peel* as raw material in gas stripping method for the first time. Such convenient, reliable and environment friendly way ensured the high graphitization degree and specific surface area, contributing to the combination of temperature control and activating agent KHCO₃. 2D/2D GS/CN-2 nanosheet was successfully synthesized with the remarkable GS-4-1100 and melamine, possessing higher photocatalytic activity with 5.49wt% in-situ Cu NPs for hydrogen production from water splitting. The special pore structure controlled by the adding ratio of KHCO₃ and melamine had great impact on carrier mobility and efficient separation of electron pairs, the key factor for photocatalysis activity. In addition, GS/CN-2 performed a slow steady increase photocatalysis activity during the 5 cycle of measurement. This work provides a reliable and expedite way to compound few layered graphene nanosheet composite with high photocatalysis hydrogenation activity derived from biomass waste.

EXPERIMENTAL SECTION

Preparation of GS.

The *pomelo peel* was cleaned with deionized water for three times and dried at 100 °C for 6h in a vacuum drying oven, and then the yellow solid with sweet perfume was grounded to obtain the *pomelo peel* powder. 29.1 g aforesaid powder was heated to 500 °C for 2 h at a heating rate of 1 °C min⁻¹ under nitrogen atmosphere and subsequently raised the calcination temperature to 800 °C

for 1 h at the heating rate of 3 °C min⁻¹ in the tube furnace. The carbonized materials were cooled down to room temperature at the rate of 5 °C min⁻¹ and then cleaned with deionized water for three times, and dried at 80 °C in conventional oven overnight, resulting in 5.0 g black power. The obtained material was uniformly mixed with KHCO₃ power (the mass ratios of KHCO₃ to carbonized materials was 2:1, 3:1, 4:1, 5:1 and 6:1) placed in KH250DE-type ultrasonic cleaner (HECHAUNG ultrasonic instrument co. LTD) and stirred in a constant temperature magnetic stirrer for 1 h after grinding with agate mortar for 30 min. The as-prepared black power was put into the tube furnace and heated to 800 °C for 2 h and therewith raised to the activation temperature (1000 °C, 1100 °C and 1200 °C) for 1 h with a heating rate of 3 °C min⁻¹ under a nitrogen atmosphere, cooling down to the room temperature at the rate of 5 °C. The obtained samples were cleaned with diluted HCl solution (0.1 mol L⁻¹) and deionized water for three times respectively to remove residual inorganic impurities until reaching to a pH value of 7, followed by drying at 80 °C in a vacuum drying oven overnight and reserved for later. The final product was obtained and denoted as GS-X-Y where X represented the KHCO₃/C weight ratio in g/g and Y referred to graphitization temperature in °C.

GS/CN nanosheets synthetic procedures.

150 mg melamine uniformly mixed with GS (10 mg, 30 mg, 50 mg, 70 mg and 90 mg) was placed in KH250DE-type ultrasonic cleaner and stirred in a constant temperature magnetic stirrer for 1 h after grinding with agate mortar for 30 min. The as-obtained samples were put into the tube furnace and annealed at 550 °C in a muffle furnace for 4 h accompanied by a heating rate of 10 °C min⁻¹ under nitrogen atmosphere, cooling down to the room temperature at the rate of 5 °C. Bulk g-C₃N₄ was prepared from melamine according to a standard literature method.⁶⁵ Briefly, 5.00 g of melamine only was annealed at above condition to obtain 0.75 g yellow solid, yield in 15%. Since the mass of graphene achieved constant weight during the synthesis process of GS/CN after graphitization, the theoretical content of GS in the samples is 30.77%, 57.14%, 68.97%, 75.68% and 80.00 wt% respectively. And the mass of the output was as stated above. The collected samples were donated as GS/CN-1, GS/CN-2, GS/CN-3, GS/CN-4, GS/CN-5 respectively. For reference, a sample which was uniformly mixed up with 30 mg GS and 22.5 mg g-C₃N₄ was prepared without further processing, corresponding to GS/CN-2 and donating as sample GS+g-C₃N₄.

Enhancing Photocatalytic hydrogen evolution with GS/CN

The photocatalytic experiments were carried out in a Pyrex reactor (300 mL) with airtight gas circulation, connecting to an evacuation system. Without further processing, the photocatalysts was added into the reactor with 10 mL lactic acid as sacrificial electron donor, 10 mL 2 mmol L⁻¹ copper acetate solution and 50 mL deionized water in standard procedure. GS/CN/Cu nanocomposite was synthesized by in situ photoreduction method.⁵¹ Different volumes of 2 mmol L⁻¹ copper acetate solution (0 mL, 2 mL, 4 mL, 6 mL, 8 mL, 10 mL and 12 mL), 10 mL lactic acid and 10 mg GS/CN were added into the reactor, and then corresponding volume of deionized water was added (58 mL, 56 mL, 54 mL, 52 mL, 50 mL and 48 mL, respectively) to ensure the volume of liquid added was 70 mL. And the theoretical content of Cu NPs in GS/CN/Cu could be 0wt%, 1.83wt%, 3.66wt%, 5.49wt%, 7.31wt%, 9.14wt% and 10.97wt%, respectively. The aqueous solution, stirring with magneton, was irradiated by a 300 W Xe lamp (PLS-SXE 300CUV, Perfect light. Co. Ltd., Beijing) with a visible light intensity of 158 m W cm⁻² after completely degassing for 1 h without any filter. At the meantime, in order to keep the temperature of reaction system at room temperature, a flow of cooling water is employed. During irradiation time, macroscopic Cu NPs were generated on the

surface of GS/CN when 15.6 mL 2 mmol L⁻¹ copper acetate solution was added, and GS/CN was reduced at the same time. The theoretical Cu NPs content in GS/CN/Cu is 11.35wt%, 20.38wt%, 27.74wt%, 33.86wt%, 39.02wt% and 50.00wt%, respectively. Online gas chromatography (Tian Mei, GC-7900, 5 Å molecular sieve column, nitrogen as a carrier gas) was used to determine the hydrogen evolution with nitrogen as carrying gas in the system, connecting to a thermal conductivity detector (TCD).

Characterization

Raman spectra were collected by Laser Confocal Raman Microscopy system (Lab RAM Aramis, H.J.Y., France), exciting at the wavelength of 532 nm.

In order to characterize the variety structure of the materials, X-ray diffraction (XRD) (Bruker D8 Advance) measurements were carried out using graphite monochromatized Cu-K α ($\lambda = 1.5406 \text{ \AA}$) radiation, in which the 2θ range from 5° to 80°.

Fourier transform infrared (FTIR) spectra of the samples were obtained on a Bruker Tensor 27 spectrometer, using the KBr tableting method. The Brunauer-Emmett-Teller (BET) specific surface area was based on nitrogen adsorption and desorption isotherms measured at 77 K, determining by a surface area and porosity analyzer (ASAP 2020, American).

Field-emission scanning electron microscopy (FESEM, Hitachi, S-4800) and energy-dispersive X-Ray spectroscopy (EDS) images were collected to obtain microstructural characterization and the elemental mapping of desired regions, respectively.

Transmission electron microscopy (TEM) were performed on FEI Tecnai G2 F20 TEM. The UV-vis diffuse reflectance spectra (DRS, Hitachi U-3010 spectrophotometer) were collected, with BaSO₄ as a reference, by the Kubelka-Munk approach at room temperature, ranging from 200 nm to 800 nm.

Steady-state/time-resolved photoluminescence emission spectra (320 nm excitation) were recorded with a fluorescence spectrophotometer at room temperature (Edinburgh Instruments, FLSP-920).

Acknowledgements

The authors are extremely grateful for the financial support of the research fund of the Key Laboratory of Fuel Cell Technology of Guangdong Province, the National Natural Science Foundation of China (No. 21571064).

References

1. Gamze, E.; Onur, G. A.; Tanju, K., *Science of the Total Environment* **2018**.
2. Akyüz, D.; Zunain Ayaz, R. M.; Yılmaz, S.; Uğuz, Ö.; Saroğlu, C.; Karaca, F.; Özkaya, A. R.; Koca, A., *International Journal of Hydrogen Energy* **2019**, *44* (34), 18836–18847.
3. Weiwei, F.; Yanwei, W.; Huijuan, Z.; Miaomiao, H.; Ling, F.; Xiaohui, Y.; Zhengyong, H.; Jian, L.; Xiao, G.; Yu, W., *Journal of Catalysis* **2018**.
4. Yimei, Y.; Baoshan, H.; Wenbin, Z.; Qian, Y.; Feng, Y.; Juncong, R.; Xiaogang, L.; Yan, J.; Liang, F.; Qingjiang, P., *Electrochimica Acta* **2019**.
5. Luo, D.; Zheng, Q.; Zhang, Z.; Guo, Z.; Wei, X.; Zhen, W.; Zhang, X., *International Journal of Hydrogen Energy* **2019**, *44* (52), 28123–28133.
6. Sk, R.; Tarik, A.; Sushil, K.; Gilbert, D. N.; Kaushik, G., *ChemCatChem* **2019**.

7. Hoang, C. V.; Hayashi, K.; Ito, Y.; Gorai, N.; Allison, G.; Shi, X.; Sun, Q.; Cheng, Z.; Ueno, K.; Goda, K.; Misawa, H., *Nat Commun* **2017**, *8* (1), 771.
8. Li, X.; Yu, J.; Wageh, S.; Al-Ghamdi, A. A.; Xie, J., *Small* **2016**, *12* (48), 6640–6696.
9. Qin, J.; Zeng, H., *Applied Catalysis B: Environmental* **2017**, *209*, 161–173.
10. Li, H.; Wang, Y.; Chen, G.; Sang, Y.; Jiang, H.; He, J.; Li, X.; Liu, H., *Nanoscale* **2016**, *8* (11), 6101–9.
11. Diab, K. R.; El-Maghrabi, H. H.; Nada, A. A.; Youssef, A. M.; Hamdy, A.; Roualdes, S.; Abd El-Wahab, S., *Journal of Photochemistry and Photobiology A: Chemistry* **2018**, *365*, 86–93.
12. Wei, F.; Liu, Y.; Zhao, H.; Ren, X.; Liu, J.; Hasan, T.; Chen, L.; Li, Y.; Su, B. L., *Nanoscale* **2018**, *10* (9), 4515–4522.
13. Rivero, M. J.; Iglesias, O.; Ribao, P.; Ortiz, I., *International Journal of Hydrogen Energy* **2019**, *44* (1), 101–109.
14. Hafeez, H. Y.; Lakhera, S. K.; Bellamkonda, S.; Rao, G. R.; Shankar, M. V.; Bahnemann, D. W.; Neppolian, B., *International Journal of Hydrogen Energy* **2018**, *43* (8), 3892–3904.
15. Liu, X.; Xu, S.; Chi, H.; Xu, T.; Guo, Y.; Yuan, Y.; Yang, B., *Chemical Engineering Journal* **2019**, *359*, 1352–1359.
16. Xiang, Q.; Yu, J.; Jaroniec, M., *The Journal of Physical Chemistry C* **2011**, *115* (15), 7355–7363.
17. Zeng, J.; Song, T.; Lv, M.; Wang, T.; Qin, J.; Zeng, H., *RSC Advances* **2016**, *6* (60), 54964–54975.
18. Xue, W.; Hu, X.; Liu, E.; Fan, J., *Applied Surface Science* **2018**, *447*, 783–794.
19. Qin, J.; Huo, J.; Zhang, P.; Zeng, J.; Wang, T.; Zeng, H., *Nanoscale* **2016**, *8* (4), 2249–59.
20. Zhao, X.; Pan, D.; Chen, X.; Li, R.; Jiang, T.; Wang, W.; Li, G.; Leung, D. Y. C., *Applied Surface Science* **2019**, *467–468*, 658–665.
21. Zhu, Z.; Zhou, F.; Zhan, S.; Huang, N.; He, Q., *Applied Surface Science* **2018**, *456*, 156–163.
22. Xiao, Z.; Jiang, W.; Qifen, L.; Yongfeng, Q.; Zheng, J.; Ping, H.; Xuemei, Q.; Pengfei, S.; Qingwei, L.; Jianxing, R., *Chemical Engineering Journal* **2017**.
23. Wan, D. Y.; Zhao, Y. L.; Cai, Y.; Asmara, T. C.; Huang, Z.; Chen, J. Q.; Hong, J.; Yin, S. M.; Nelson, C. T.; Motapothula, M. R.; Yan, B. X.; Xiang, D.; Chi, X.; Zheng, H.; Chen, W.; Xu, R.; Ariando; Rusydi, A.; Minor, A. M.; Breese, M. B. H.; Sherburne, M.; Asta, M.; Xu, Q. H.; Venkatesan, T., *Nat Commun* **2017**, *8*, 15070.
24. Liang, W.; Xuan, H.; Muen, H.; Lai, L.; Tong, L.; Yaowen, G.; Qingyi, Z.; Chun, H., *Applied Catalysis B: Environmental* **2019**.
25. Jin, R.; Ting, P.; Yuying, W.; Chengquan, C.; Peng, C.; Pengpeng, Z.; Xinyu, A.; Cen -Feng, F.; Zhengjin, Y.; Tongwen, X., *Angewandte Chemie International Edition* **2019**.
26. Naidu, P. P.; Gujjala, R.; Shakuntala, O.; Banoth, P., *Journal of Applied Polymer Science* **2019**.
27. Li; Jiajie; Zhang; Yumin; Zhang; Xinghong; Han; Jiecai; Wang; Yi; Gu; Lin; Zhang; Zhihua; Wang; Xianjie; Jian; Jikang; Xu; Ping; Song; Bo, *ACS Applied Materials & Interfaces* **2015**.
28. Mei, L.; Shaojie, W.; Wei, C.; Li, G.; Xiyang, L.; Liqun, M.; Haifeng, D., *Journal of the Chinese Chemical Society* **2019**.
29. baojiang, j.; yuqing, h.; qing, y.; haijing, y.; yunqi, t.; shuai, c.; zheyang, y.; chungui, t., *ChemCatChem* **2017**.
30. Yuqing, H.; Qing, Y.; Haijing, Y.; Yunqi, T.; Shuai, C.; Zheyang, Y.; Chungui, T.; Baojiang, J., *ChemCatChem* **2017**.
31. Al-Gaashani, R.; Najjar, A.; Zakaria, Y.; Mansour, S.; Atieh, M. A., *Ceramics International* **2019**.
32. Peng, W.; Han, G.; Huang, Y.; Cao, Y.; Song, S., *Results in Physics* **2018**, *11*, 131–137.
33. Yang, H.; Min, S.; Xin, X.; Chunbao, S.; Jue, K., *Applied Surface Science* **2019**.
34. Li, B. W.; Luo, D.; Zhu, L.; Zhang, X.; Jin, S.; Huang, M.; Ding, F.; Ruoff, R. S., *Adv Mater* **2018**, *30* (10).

35. Afzal, K. ; Sk Masiul, I. ; Shahzad, A. ; Rishi, R. K. ; Mohammad, R. H. ; Kun, H. ; Ming, H. ; Xuegong, Y. ; Deren, Y., *Advanced Science* **2018**.
36. Kai, L. ; Hongji, L. ; Mingji, L. ; Cuiping, L. ; Lin, S. ; Lirong, Q. ; Baohe, Y., *Composites Science and Technology* **2019**.
37. Naghdi, S. ; Rhee, K. Y. ; Kim, M. T. ; Jaleh, B. ; Park, S. J., *Carbon Letters* **2016**, *18*, 37–42.
38. Sergio, F.-G. ; Manfred, R. ; Guanhui, G. ; Lauren, A. G. ; Bharat, S. ; Pierre, C. ; Gabriele, C. ; Ziani de Souza, S. ; Carsten, P. ; Achim, T. ; João Marcelo, J. L. ; Oliver, B. ; Lutz, G., *Nano Letters* **2017**.
39. Yan, S. ; Zhong-Liu, L. ; Cai, C. ; Xu, W. ; Hang, L. ; Chen, L. ; Jia-Ou, W. ; Shi-Yu, Z. ; Yu-Qi, W. ; Dong-Xia, S. ; Kurash, I. ; Jia-Tao, S. ; Ye-Liang, W. ; Hong-Jun, G., *Nano Letters* **2018**.
40. Pranay, R. ; Shweta, A. ; Apurva, S. ; Rao, T. R. ; Jayakumar, B. ; Ajay, D. T., *Scientific Reports* **2018**.
41. Rekha, M. Y. ; Nitin, M. ; Chandan, S., *Scientific Reports* **2018**.
42. Xie, G. ; Zhang, K. ; Guo, B. ; Liu, Q. ; Fang, L. ; Gong, J. R., *Adv Mater* **2013**, *25* (28), 3820–39.
43. Haoran, Y. ; Huibing, C. ; Denian, L. ; Lifang, D. ; Jian, C. ; Yukun, F. ; Mingyang, H. ; Fuan, S., *Electrochemistry Communications* **2019**.
44. Yao, L. ; Simin, L. ; Yeru, L. ; Yong, X. ; Hanwu, D. ; Mingtao, Z. ; Hang, H. ; Yingliang, L., *ACS Sustainable Chemistry & Engineering* **2019**.
45. Zhongxin, S. ; Mingtao, Z. ; Hang, H. ; Hanwu, D. ; Yeru, L. ; Yong, X. ; Bingfu, L. ; Yingliang, L., *Chemical Engineering Journal* **2017**.
46. Danyang, W. ; Chao, Z. ; Yantao, S. ; Hongyu, J. ; Jinwen, H. ; Xuedan, S. ; Duanhui, S. ; Suxia, L. ; Ce, H., *ACS Sustainable Chemistry & Engineering* **2018**.
47. Yoon, S.-H. ; Lim, S. ; Song, Y. ; Ota, Y. ; Qiao, W. ; Tanaka, A. ; Mochida, I., *Carbon* **2004**, *42* (8–9), 1723–1729.
48. Laura, G. ; Loreto, S. ; Nausika, Q. ; Viliam, V. ; Peter, K. ; Viera, S. ; Teresa, A. C., *Electrochimica Acta* **2018**.
49. Masoud, A. ; Farhad, G., *Journal of Electroanalytical Chemistry* **2019**.
50. Zhang, P. ; Song, T. ; Wang, T. ; Zeng, H., *Applied Catalysis B: Environmental* **2018**, *225*, 172–179.
51. Zhang, P. ; Song, T. ; Wang, T. ; Zeng, H., *Applied Catalysis B: Environmental* **2017**, *206*, 328–335.
52. Zhang, P. ; Wang, T. ; Zeng, H., *Applied Surface Science* **2017**, *391*, 404–414.
53. Zhang, P. ; Song, T. ; Wang, T. ; Zeng, H., *International Journal of Hydrogen Energy* **2017**, *42* (21), 14511–14521.
54. Song, T. ; Zhang, P. ; Zeng, J. ; Wang, T. ; Ali, A. ; Zeng, H., *ChemCatChem* **2017**, *9* (21), 4035–4042.
55. Huang, T. ; Xu, Z. ; Zeng, G. ; Zhang, P. ; Song, T. ; Wang, Y. ; Wang, T. ; Huang, S. ; Wang, T. ; Zeng, H., *Carbon* **2019**, *143*, 257–267.
56. Zhao, D. ; Dai, Y. ; Chen, K. ; Sun, Y. ; Yang, F. ; Chen, K., *Journal of Analytical and Applied Pyrolysis* **2013**, *102*, 114–123.
57. Trubetskaya, A. ; Larsen, F. H. ; Shchukarev, A. ; Ståhl, K. ; Umeki, K., *Fuel* **2018**, *225*, 89–94.
58. Lozano-Castello, D. ; Calo, J. M. ; Cazorla-Amoros, D. ; Linares-Solano, A., *Carbon* **2007**, *45* (13), 2529–2536.
59. Chen, W. Q. ; Veksha, A. ; Lisak, G., *Carbon* **2020**, *159*, 378–389.
60. Si-Yu, L. ; Qi-Shi, D. ; Shu-Qing, W. ; Pei-Duo, T. ; Da-Peng, L. ; Ri-Bo, H., *Journal of Cleaner Production* **2019**.
61. Esmaeili; Entezari; M, H., *Journal of Colloid and Interface Science* **2014**.
62. Wan, S. ; Ou, M. ; Zhong, Q. ; Cai, W., *Carbon* **2018**, *138*, 465–474.
63. Xu, J. ; Ao, Y. ; Fu, D. ; Yuan, C., *J Colloid Interface Sci* **2008**, *328* (2), 447–51.
64. Keun Soo, K. ; Yue, Z. ; Houk, J. ; Sang Yoon, L. ; Jong Min, K. ; Kwang, S. K. ; Jong-Hyun, A. ; Philip, K. ; Jae-Young, C. ; Byung Hee, H., *Nature* **2009**.
65. Song, T. ; Zhang, P. ; Wang, T. ; Ali, A. ; Zeng, H., *Applied Catalysis B: Environmental* **2018**, *224*, 877–

885.

66. Liu, H. ; Wang, T. ; Zeng, H., *Particle & Particle Systems Characterization* **2015**, *32* (9), 869–873.